Editors' Suggestion

Design, realization, and testing of a brazing-free C-band radio frequency photogun

D. Alesini,* F. Cardelli, G. Di Raddo, L. Faillace, M. Ferrario, A. Gallo, A. Giribono, G. Latini, S. Lauciani, A. Liedl, L. Pellegrino, L. Piersanti, S. Pioli, J. Scifo, B. Serenellini, G. J. Silvi, L. Spallino, A. Vannozzi, and C. Vaccarezza
INFN-LNF, Frascati, Italy

L. Ficcadenti
INFN-Roma, Rome, Italy and SBAI, Sapienza University of Rome, Rome, Italy

T. G. Lucas, L. Hol, and P. Craievich
Paul Scherrer Institut, Villigen, Switzerland

(Received 20 June 2025; accepted 27 October 2025; published 12 January 2026)

Radio frequency (rf) photoguns are widely used in modern particle accelerator facilities, particularly in free electron lasers (FELs), as they provide very low-emittance, high-brightness electron bunches. Presently, the rf technology mostly used for photoguns is the S-band (∼3 GHz), with typical cathode peak fields of 80–120 MV/m and maximum repetition rates of ∼100 Hz. According to beam dynamics studies, the higher the peak electric fields on the cathode, the better the quality of the beam emerging from the gun. In this respect, S-band rf guns represent the state-of-the-art, both in terms of reachable cathode peak fields and repetition rates. An innovative C-band rf gun, operating at 5.712 GHz and aiming at reaching cathode peak fields larger than 160 MV/m, with repetition rates exceeding 400 Hz, has been designed, realized, and high-power tested. Its device consists of a 2.5-cell standing wave (SW) cavity with a four-port mode launcher whose overcoupled design allows it to operate with short rf pulses (300 ns). Its realization has been based on the new brazing-free technology developed and successfully tested at the Frascati Laboratories of the National Institute of Nuclear Physics (INFN-LNF, Italy). In the paper, we illustrate the design and realization performed by INFN-LNF, and its high-power rf test, which was conducted at the C-band test facility at the Paul Scherrer Institute (Switzerland).

DOI: 10.1103/jrth-j9sf

I. INTRODUCTION

The achievable beam brightness in rf photoinjectors is strongly dependent on the cathode peak field [1]. For this reason, in the last generation rf guns, a great deal of effort has been put into increasing the field amplitude while keeping the breakdown rate (BDR) under control [2]. Values greater than the present 120 MV/m S-band state-of-the-art cathode peak field are extremely desirable to further improve the beam quality. In this context, the possibility of implementing a full C-band injector is highly attractive with respect to achievable beam parameters [3], system compactness, and the ability to operate at high repetition rates, as proposed for the X-band linacs of the EuPRAXIA@SPARC_LAB project [4] and XLS design study [5].

The ability to operate at higher repetition rates is mainly related to the filling time reduction in case of SW cavities, corresponding to an rf pulse duration shortening, which scales as $f^{-3/2}$, and to the increase in the rf structure efficiency (the shunt impedance per unit length), which scales as $f^{1/2}$. These allow a saving of rf power to reach the design cathode peak electric field and, as a consequence, higher efficiency, lower average dissipated power, and possibility to reach repetition rates in the 400–1000 Hz range. In addition, the C-band frequency regime is a more recent technology whose reliability and effectiveness have been already fully demonstrated. Successful FEL radiation facilities such as SwissFEL [6] (Switzerland) and SACLA [7] (Japan) are based on linacs made of C-band traveling-wave accelerating sections. The technology is industrially mature, since power sources and the needed ancillary components (driver amplifiers, waveguides, ceramic windows, dummy loads, LLRFs, isolators, and pulse compressors) are all commercially available. However, beam injectors fully based

*Contact author: alesini@lnf.infn.it

Published by the American Physical Society under the terms of the Creative Commons Attribution 4.0 International license. Further distribution of this work must maintain attribution to the author(s) and the published article's title, journal citation, and DOI.

on this technology are yet to be developed. The development of a C-band photogun is also extremely attractive for its possible applications in upgrades of existing photoinjectors for FELs.

In this paper, we describe the design, realization, and high-power test of a C-band SW rf photogun. The electromagnetic and thermo-mechanical design of the device is illustrated in the first two sections of this paper. In the third section, we present the realization procedure and the final assembly, while the fourth and fifth sections report the results of the low and high rf power tests, respectively.

The realization and test of this new photogun have been funded by the European Union in the framework of the I.FAST project [8] and by INFN Commission V. The gun has been designed to minimize all the electromagnetic quantities that are hypothesized to increase the BDR, such as the peak surface electric field E_s, the modified Poynting vector [9], the rf pulse length, and pulsed heating [10] and has been realized with the new technology developed at INFN [11]. Traditional rf gun fabrication processes rely on brazing, which requires the use of large vacuum furnaces. This makes the method not only very expensive but also introduces a significant risk of failure. Moreover, brazing induces copper thermal stress release, which has been correlated with an increased BDR in X-band prototypes. By avoiding brazing, these stress-related issues can be eliminated, thereby reducing BDR [12]. In addition, experimental evidence suggests that brazing-free approaches may shorten the conditioning time of hard copper structures when compared to annealed copper [13]. This represents an important operational advantage in terms of efficiency and reliability. To exploit these benefits, a novel brazing-free fabrication technique has been developed at LNF-INFN. The method, based on the use of special rf-vacuum gaskets, has already been successfully applied for the realization of rf photoguns in S-band [14–16].

II. ELECTROMAGNETIC DESIGN

The photogun is a 2.5-cell SW structure operating on the π-mode [17–19]. In the design of the gun, we have considered all the quantities that allow us to keep the BDR in rf structures under control: the peak surface E field (E_{surf}), the modified Poynting vector (S_c) [9], the rf pulse length (t_{imp}), and pulsed heating (ΔT) [10]. The first two quantities have been minimized adopting an elliptical profile of the irises. Large iris apertures have been adopted to increase the frequency separation between the π working mode and the nearest $\pi/2$-mode, thus avoiding excitation of this second mode during operation with short rf pulses. Large apertures also allow one to increase the pumping speed on the cathode cell. The optimized 2D-profile of the gun's cells with its main dimensions is depicted in Fig. 1, while the gun parameters are reported in Table I. In the table, the filling time was calculated (and experimentally measured) using the

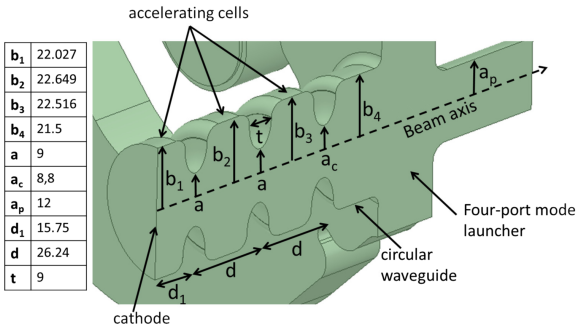

FIG. 1. Optimized cell profile with main dimensions.

standard expression $\tau_F = 2Q_L/\omega_{\mathrm{rf}}$, where the loaded quality factor is given by $Q_L = Q_0/(1+\beta)$.

The rf pulse length and pulsed heating have been minimized with a proper choice of the coupling coefficient (β) and with an on-axis electrical coupler. The required input power (P_{in}) to reach a cathode peak field (E_{cath}) of 160 MV/m, and the reflected one (P_{refl}), as a function of β, are given in Fig. 2(a) for different rf pulse lengths. Figure 2(b) shows the corresponding average dissipated power (P_{av}) for a 400 Hz repetition rate operation. We have chosen a coupling coefficient β equal to 3, as a good compromise that allows to keep the required power below 20 MW with a 300 ns input pulse, and an average dissipated power of 1 kW in the 400 Hz repetition rate case. These values of power and repetition rate are those of modulator and klystron available on the market [20].

Standard magnetic couplers, even if strongly rounded [15,17,21], could not be adopted because of the high magnetic field and, as a consequence, high pulsed surface heating on the coupling holes. For this reason, a four-port mode launcher-type coupler has been adopted [18,22–24]. This type of coupler allows to strongly reduce the pulsed surface heating due to the electrical coupling, which

TABLE I. Main C-band gun parameters (measured values are shown in parentheses when different from the calculated ones).

Working frequency [GHz]	5.712
$E_{\mathrm{cath}}/P_{\mathrm{diss}}^{1/2}$ [MV/(mMW$^{1/2}$)]	51.4
rf input power [MW]	18 (19)
Cathode peak field [MV/m]	160
Cathode type	Copper
Repetition rate [Hz]	400
Unloaded quality factor (Q_0)	11,900
Shunt impedance [MΩ]	3.48
Filling time (τ_F) [ns]	166 (147)
Coupling coefficient (β)	3 (3.5)
rf pulse length t_{imp} [ns]	300
$E_{\mathrm{surf}}/E_{\mathrm{cath}}$	0.96
Modified Poynting vector (S_c) [W/μm^2]	2.5
Pulsed heating (ΔT) [°C]	16
Average dissipated power [W]	1000

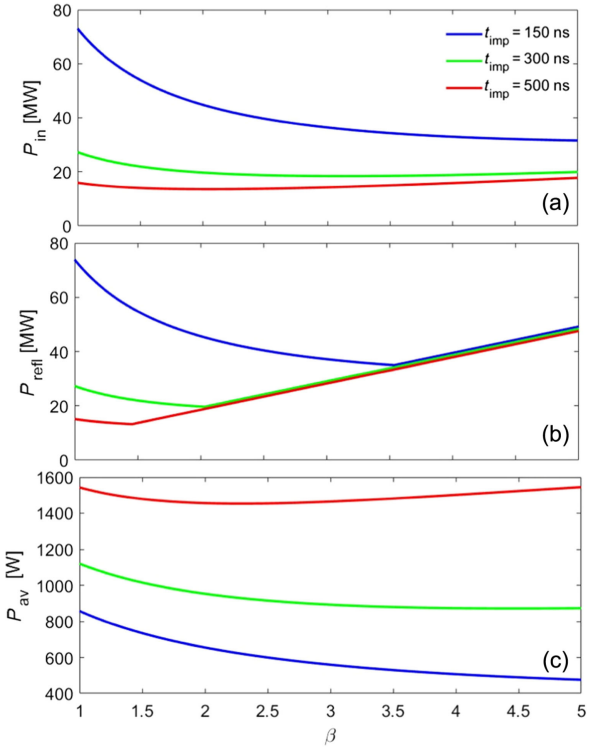

FIG. 2. (a) Input power (P_{in}), (b) reflected power (P_{refl}), and (c) average dissipated power (P_{av}), as a function of β and for different rf pulse lengths t_{imp}, to reach a cathode peak field of 160 MV/m (case of a perfect square profile of the rf input power at 400 Hz).

perfectly compensates the dipole and quadrupole field components in the coupler region. The mode launcher, whose design was performed with ANSYS HFSS [25], also features two integrated pumping ports. The electromagnetic model of the photogun with the four-port mode launcher is illustrated in Fig. 3. The magnitude and phase of the longitudinal electric field on axis are reported in Fig. 4. This plot put in evidence that the accelerating field is a perfect standing wave in the accelerating cells, while in the

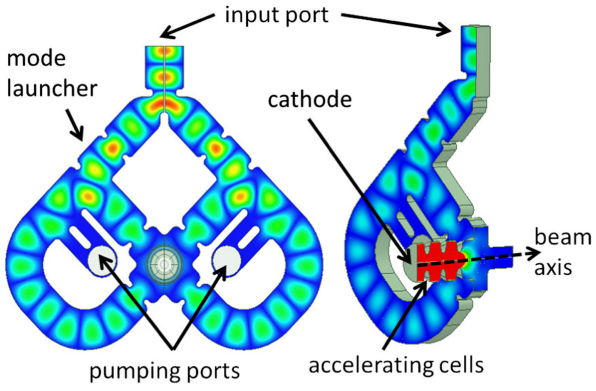

FIG. 3. Electromagnetic model of the C-band gun with four-port mode launcher.

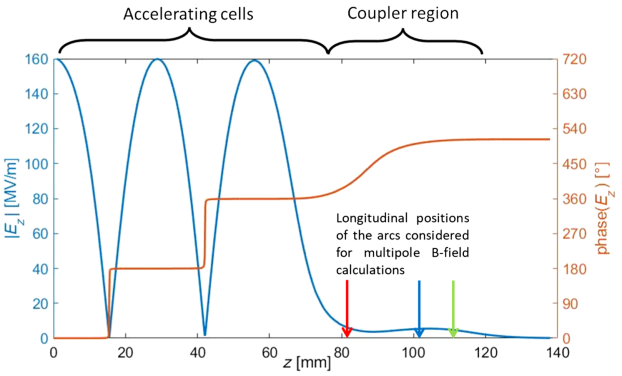

FIG. 4. Longitudinal electric field on axis.

coupler region it has a residual traveling wave component (nonconstant phase), related to the power flow from the input coupler waveguide into the device. The effect of these traveling wave components on the beam dynamics has been carefully studied also in the case of long circular waveguides [3,26] and does not noticeably affect the beam dynamics.

The magnitude of the magnetic field as a function of the azimuthal coordinate (θ), on three different arcs with a radius of 5 mm in the mode launcher region, is depicted in Fig. 5. The arcs are in the center of the mode launcher itself (corresponding to the $z = 102$ mm longitudinal coordinate of Fig. 4), in the center of the circular waveguide between the mode launcher and the first iris ($z = 82$ mm) and at the beginning of the output beam pipe ($z = 112$ mm). The plot illustrates that the residual quadrupole component is completely negligible, while there is an octupole component that vanishes moving toward the circular waveguide. For a given arc, it is possible to verify that the phase of the field is constant as a function of the azimuthal coordinate and, for this reason, it is possible to perform a spatial Fourier analysis, according to the formula [27]:

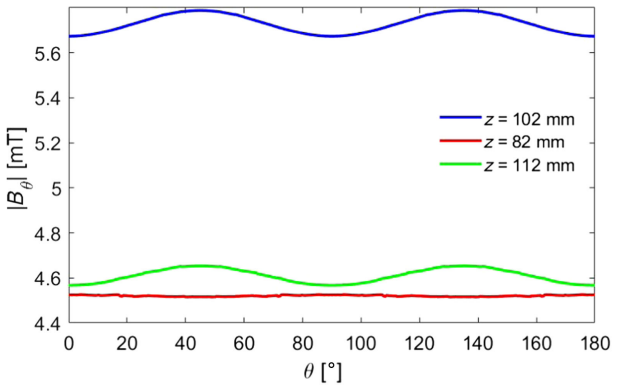

FIG. 5. Magnitude of the magnetic field as a function of the azimuthal coordinate (θ), on three different arcs with a radius of 5 mm in the mode launcher region.

$$B_\theta(r,\theta,z) \cong A_o(z)r + \sum_{n=1}^{\infty} A_n(z) e^{j\varphi_n(z)} \cos(n\theta) r^{n-1}, \quad (1)$$

where the A_n terms are the magnitude of the multipole components. The quadrupole component is associated with the term with $n = 2$, while the octupole component is associated with the term $n = 4$. Their values, at the center of the coupler, have been calculated by fitting the plots of Fig. 5 and are $A_2 < 10^{-5}$ T/m and $A_4 \approx 450$ T/m^3, respectively. Beam dynamics simulations [3,26], considering also the effect of these multipole components, have shown that their effects on the beam parameters are completely negligible.

III. THERMO-MECHANICAL DESIGN

The cooling system of the gun has been designed to operate at a repetition rate of 400 Hz compatible with existing rf C-band sources [20] and possible future upgrades of the EUPRAXIA@SPARC_LAB project [4]. With a cathode peak field of 160 MV/m, the average dissipated power is 1 kW. The gun cooling system has been designed to avoid detuning of the gun during operation and hot spots that result in nonuniform cell deformations and, consequently, an imbalance in the accelerating field or coupling variations. The design of the cooling system has been performed using the ANSYS Workbench environment [25] that allowed a full coupled thermal, structural, and electromagnetic analysis. The ANSYS model of the cooling system is given in Fig. 6. The gun cells integrate four cooling channels: three independent circuits for the cells (with an internal diameter of 7 mm) and an additional one for the cathode (with a square cross section of 100 mm^2). In each cooling pipe of the cells, it is foreseen a continuous flow of demineralized water at a rate of approximately 2.5 L/min, while for the cathode pipe a flow rate of 5 L/min

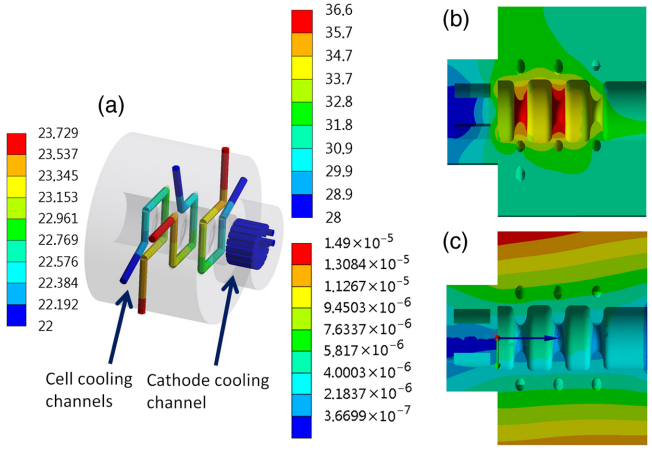

FIG. 6. (a) ANSYS model of the photogun cooling system with water temperature distribution at regime; (b) gun temperature distribution at regime; and (c) gun radial mechanical deformations (in meters) at regime.

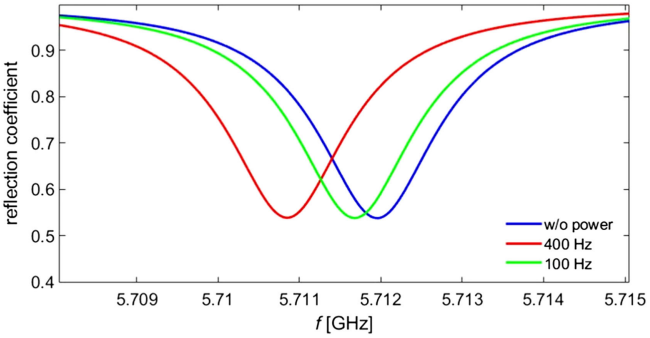

FIG. 7. Reflection coefficient at different repetition rates.

is used due to its larger cross-sectional area. The heat load obtained by the electromagnetic analysis has been imported in the thermo-mechanical module, the temperature distribution has been evaluated, and the mechanical deformations have then been calculated. The water temperature of the cooling pipes in the 400 Hz operation and the final gun temperature distribution at regime are displayed in Figs. 6(a) and 6(b). The corresponding deformations are depicted in Fig. 6(c). In the calculations, we have considered an input water temperature, and the corresponding nominal gun temperature, of 22 °C.

The deformed structure has then been simulated with the electromagnetic module. The reflection coefficient at the input port is shown in Fig. 7 for the 100 and 400 Hz cases and is compared with the ideal one (no average input power, denoted as w/o power). The plot clearly shows the detuning of the gun and the consequent resonance frequency variation due to the cavity deformation. The detuning frequency is calculated to be about 1 MHz for the gun operating at a repetition rate of 400 Hz. Such a detuning can be compensated by reducing the set water temperature by −10 °C during operation. From the electromagnetic simulation, we have also verified that the field distribution is negligibly affected.

IV. FABRICATION AND ASSEMBLY

The 3D mechanical layout of the whole photogun is shown in Fig. 8. The gun is followed by a solenoid, for emittance compensation [3], and by the laser injection chamber, which allows the last mirror reflecting the laser pulse on the cathode to be in air. Two pumping ports are integrated in the mode launcher and are connected to NEXTorr Z100 NEG/ion pumps [28].

As described above, the gun has been realized with the new brazing-free technology developed at INFN. The SW cells and cathode have been machined using the lathe Schaublin 225 TM-CNC to complete the finishing of the surfaces. The internal dimensions of the cells have been machined to within a precision of ±2 μm and a surface roughness below 30 nm [19]. The water pipes have been drilled into the gun cells, while the stainless steel water connectors have been screwed directly into the copper, with

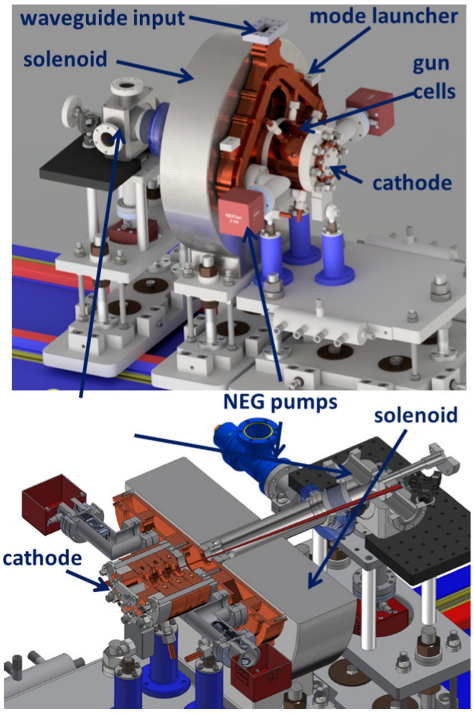

FIG. 8. Photoinjector mechanical layout with main components.

copper gaskets ensuring proper water sealing. Pictures of the machined cells before the final assembly are reported in Fig. 9. In the same figure also the gaskets used for their final assembly are shown. In the picture two gaskets are visible: a copper one and an aluminum one. Unlike [14], where a single copper gasket ensured both rf contact and vacuum seal, the C-band gun adopts a dual-gasket geometry: the external aluminum gasket for vacuum tightness and the internal copper gasket for rf contact. This solution allows the use of softer forged copper, since the aluminum gasket provides the sealing function. The main drawback is the possible formation of an air pocket between the two gaskets, which could compromise ultrahigh-vacuum operation. To avoid this, the region is evacuated through small channels connecting it to the vacuum side. The two configurations are given in Fig. 10. After the machining,

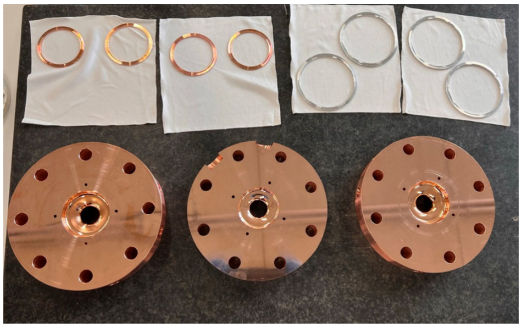

FIG. 9. Machined gun cells with gaskets.

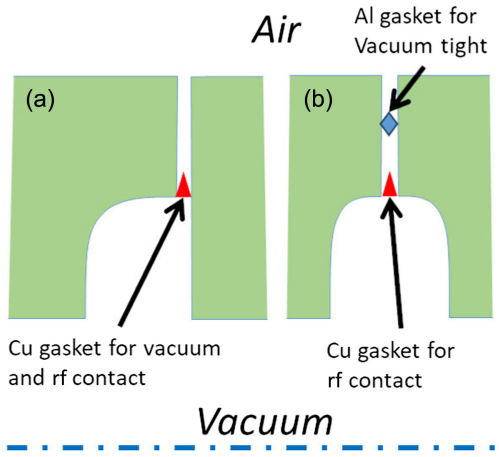

FIG. 10. Schematic of the gasket configurations used for brazing-free rf guns: (a) configuration used in S-band guns; (b) configuration used in the new C-band gun.

the cells have been cleaned using a bath of Almeco, followed by an NGL cleaning at 50 °C and a final treatment in citric acid at 40 °C to remove the oxidation. They have been finally washed with demineralized water in an ultrasonic bath and dried with pure nitrogen. After cleaning, the cells have been also heated in a vacuum furnace at 200 °C for 2 h to remove the residual water from the surfaces.

The mode launcher has been machined using the five axis milling machine Micron UCP600 Vario with precision on the internal dimensions of ±8 μm and roughness below 200 nm. It has then been brazed in a vacuum furnace using palcusil 5 alloy. Pictures of the machined mode launcher before and after brazing are given in Fig. 11. After brazing, it has been vacuum tested.

Figure 12 illustrates the mounting procedure of the cells on the gun for the final assembly. Throughout the entire process, the gun has been flushed with dry nitrogen. The mounting procedure foresaw the use of two special gaskets. The external one, in aluminum, used for a good vacuum seal, and the internal one, in copper, for the rf contact. The alignment of the cells has been guaranteed, during the mounting procedure, using two special "V" precise tools as shown in Fig. 12(c). After the final assembly, the gun has been vacuum tested with a helium leak detector with a

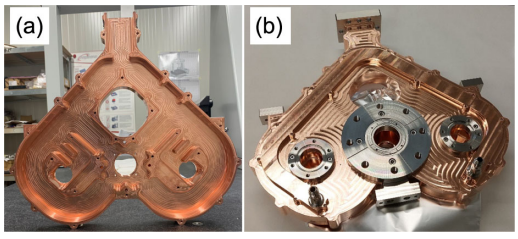

FIG. 11. Fabricated mode launcher before (a) and after brazing (b).

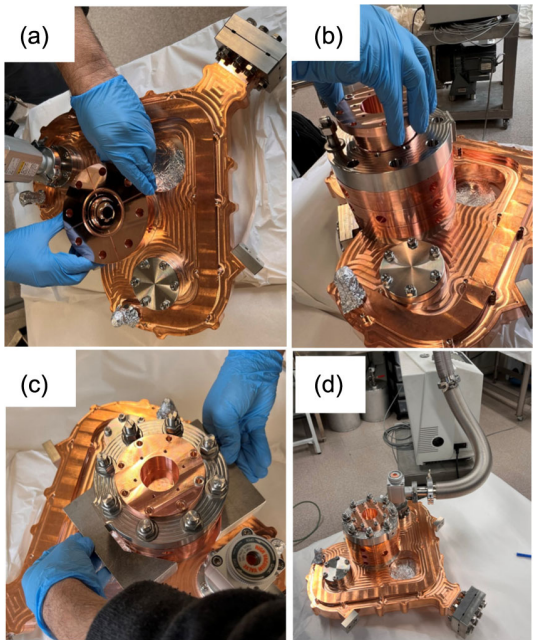

FIG. 12. Pictures of the gun under assembly: (a) assembly of the cells; (b) cathode insertion; (c) cell alignment before the final clamping; and (d) vacuum test.

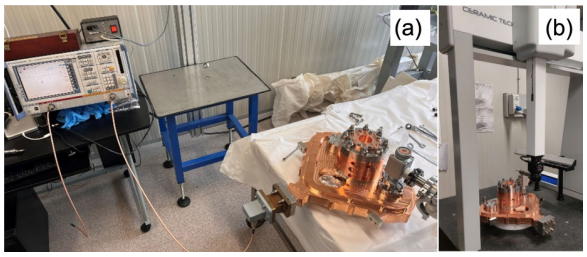

FIG. 13. Pictures of the photogun under low power rf tests (a) and mechanical characterization with coordinate measuring machines (CMM) (b).

sensitivity below 1×10^{-11} mbar/l/s. Figure 12(d) shows a picture of the final assembled gun under vacuum test. The assembled gun has been mechanically characterized, after the final assembly, using a CMM ALTERA 10.7.7 [Fig. 13(b)] and the alignment of the cells has been verified to be, in both planes, below ± 40 μm.

V. LOW POWER RF TEST RESULTS AND FINAL ASSEMBLY

The assembled gun has been tested at low power using a *R&S* ZVB 20 Network Analyzer [see Fig. 13(a)] [19]. The measurements were performed under a flux of nitrogen at constant temperature. Figure 14 reports the reflection coefficient at the gun input port. The three modes are clearly visible in the plot (the fourth mode corresponds to a mode confined in the mode launcher region with negligible

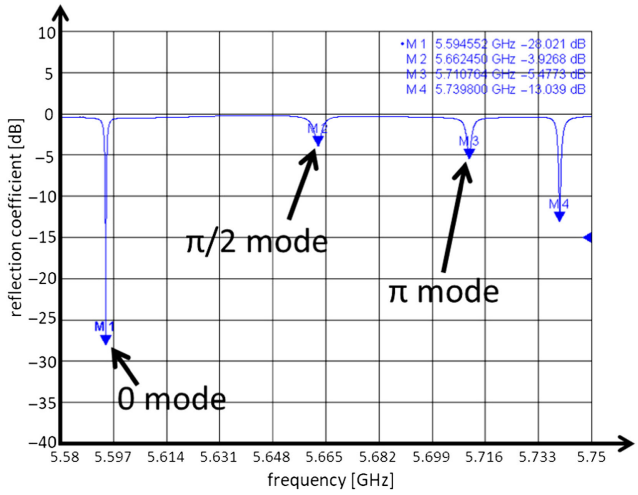

FIG. 14. Reflection coefficient at the photogun input port.

shunt impedance). The frequency of operation, quality factor, and coupling coefficient obtained by fitting the reflection coefficient are reported in Table I. They clearly show that the frequency and quality factor of the working mode are the nominal ones while the coupling coefficient is slightly larger ($\beta = 3.5$ instead of the simulated $\beta = 3$). The reason for this discrepancy is still under investigation and is probably related to the different dimensions of the first coupling iris and lower values of the cathode peak field with respect to the ideal one (as detailed below). This value of the coupling coefficient does not affect significantly the gun performance in terms of required power, rf pulse length, and cathode peak field.

The electric field on axis has been measured using a metallic bead of 2 mm diameter connected to a nylon wire, dropping into the gun. The result of this measurement is reported in Fig. 15. The field imbalance between the cells is at the level of 5%. With the bead drop technique it is not possible to measure the peak field at the cathode plane because of the effects of image currents that affect the measurement itself. The field at the cathode position has been extrapolated by a local fit of the measurements. Its value is ∼5% below the central one. The reason for this

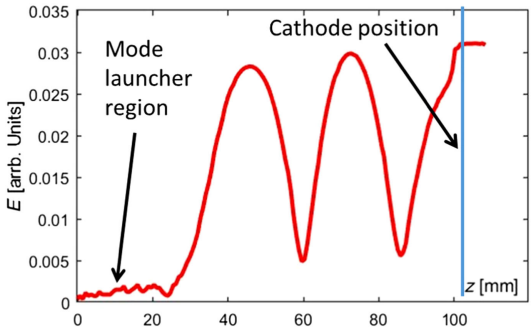

FIG. 15. Electric field profile on axis measured with the bead drop technique.

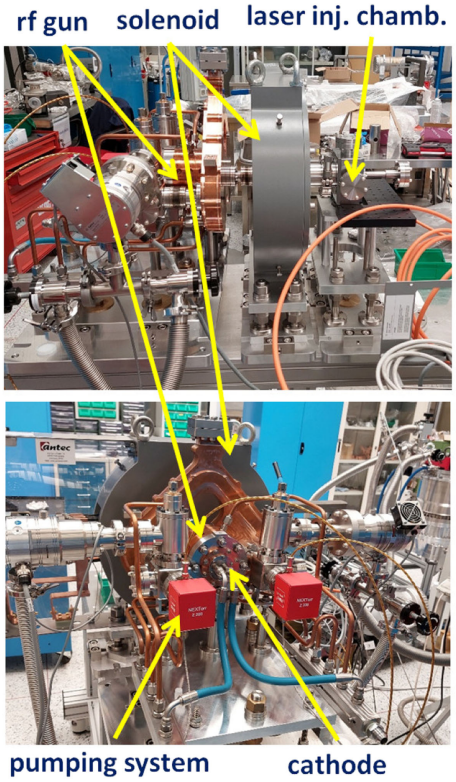

FIG. 16. Picture of the assembled injector with gun, solenoid, vacuum system, support, and vacuum chambers.

discrepancy with respect to the ideal simulated value is still under investigation and is probably due to the small deformation of the special copper gaskets used to guarantee the rf contact or not perfect compression of the gasket itself.

The gun, after the final assembly, vacuum test, and low power rf test, has been assembled in its final configuration with the solenoid and vacuum chambers, as displayed in Fig. 16.

VI. HIGH-POWER RF TEST SETUP AND RESULTS

The whole assembled photogun has been transported to PSI and installed in the high-power test stand [29]. The original gun feeding scheme foresaw the use of a new in-vacuum commercial isolator. However, this device experienced some delays due to the difficulties that have been encountered during its realization. For this reason, we have developed an alternative feeding scheme using power dividers and a BOC-type pulse compressor [30] which was already available at PSI [19].

The feeding scheme is described in Fig. 17. A four-port power splitter outputs the rf power fed in with a power ratio of 1 to 9 at the two output ports. The power from the 10% port is then compressed with the pulse compressor in order to increase the peak power. With this scheme, the reflected power from the cavity is split again with the same ratio allowing the reflected power to the klystron to be reduced to

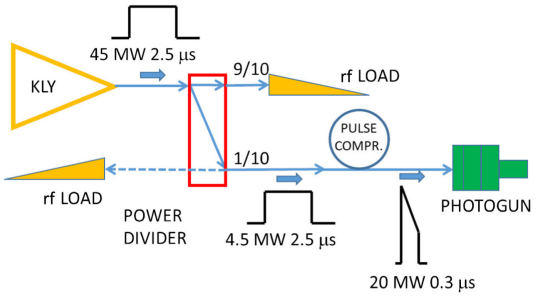

FIG. 17. Schematic layout of the feeding scheme adopted in the high-power test.

≈500 kW. The picture of the gun connected to the C-band waveguide system and ready for the high-power test is shown in Fig. 18. In the waveguide setup, there are eight combined NEG-ion pumps and four directional couplers. The vacuum was monitored through four vacuum gauges: one at the laser injection chamber, two near the BOC pulse compressor, and one near the klystron window. These have been used to monitor the local vacuum in the regions expected to suffer the most from high-power operation.

During the conditioning, an optimization of the final pseudotrapezoidal compressed pulse and pulse length has been done to simultaneously maximize the cathode peak field while keeping the reflected power to the klystron under control. The measured input and reflected power into the gun (from the directional coupler DC4) are illustrated in Fig. 19. For a comparison, in the same plot, we include the expected shapes calculated using the S-parameter measurements from the low power test. In particular, in the calculation, to fit the measured input power signal, we have considered a 46 MW peak klystron input power with 530 ns compressed pulse length and a switching time of the phase jump of 180 ns. The calculated reflected power profile shows an extremely good agreement with the measured one. We have to point out that we did not have the possibility to calibrate the measured reflected power signal and, therefore, the values reported in the plot have been normalized to the calculated ones. In all the calculations, we have considered a 10% waveguide attenuation. In the same plot, we have reported the calculated cathode peak field. From the figure, it can also be seen that the compressed pulse is 530 ns instead of the nominal 300 ns. As clarified later in the paragraph, the conditioning was limited by the reflected power to the klystron port, which caused vacuum activity in the output ceramic window. Looking at the reflected power plot, it is evident that the largest peak occurs at the end of the compressed pulse. If we consider a shorter pulse (300 ns instead of 530 ns, as reported in the figure), this reflected power increases by about 30%. This can be confirmed with numerical calculations that also take into account the passage of the reflected pulse through the BOC. Therefore, we had to slightly increase the compressed pulse length in order to reduce this reflected power at the end of the pulse.

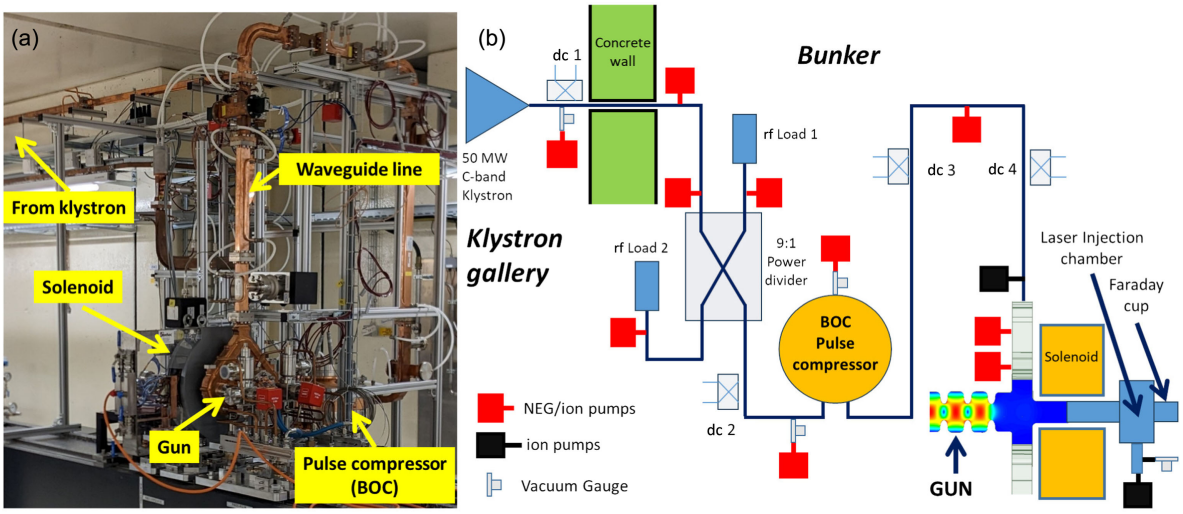

FIG. 18. (a) Picture of the realized waveguide network and installed gun; (b) schematic layout of the waveguide network.

After the first tests of the system and controls at high power in December 2023, the rf conditioning began in February 2024, once the water cooling system for the BOC was completed. The conditioning was done in a semi-automatic way, monitoring the vacuum at the different vacuum pumps and progressively increasing the power from the klystron and pulse length keeping the repetition rate at 100 Hz. In case of a vacuum discharge event, identified by a vacuum spike exceeding 3×10^{-8} mbar, the algorithm automatically interlocks the system. In the case of a reflected power to the klystron exceeding 1 MW, the system also interlocks. During the interlock, the power was set to zero and then power ramped back to the level at which the system previously interlocked. The history of the input power, converted into the peak cathode field generated in the gun, is shown in Fig. 20. Figure 21 shows the vacuum behavior as measured by the vacuum gauges distributed in the waveguide transport line and laser injection chamber. In the first phase of the conditioning (corresponding to 150 million pulses), the pulse compressor has been detuned by changing its temperature thus reducing the maximum input power into the gun. It is important to note that the conditioning has been dominated by the vacuum activity in the waveguide system and that the final maximum input power from the klystron has been limited by a vacuum activity in the ceramic of the klystron window, likely due to the reflected power from the system. In Fig. 22, we have reported the vacuum breakdown events in the gun and in the waveguide system. At the maximum

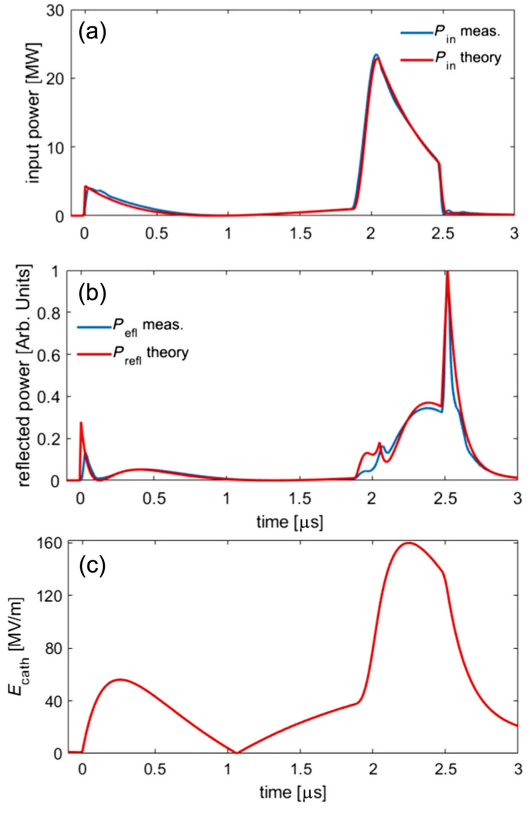

FIG. 19. Measured and calculated input (a) and reflected (b) powers into the gun (from the directional coupler DC4); and (c) calculated cathode peak field.

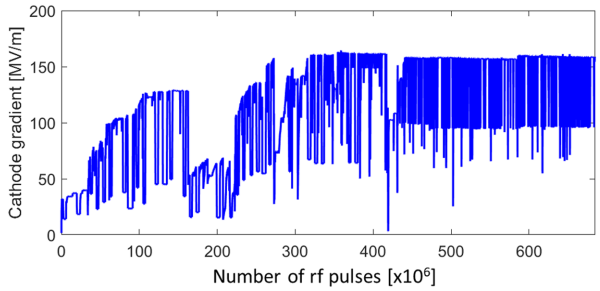

FIG. 20. Cathode field generated in the gun as a function of the rf pulses.

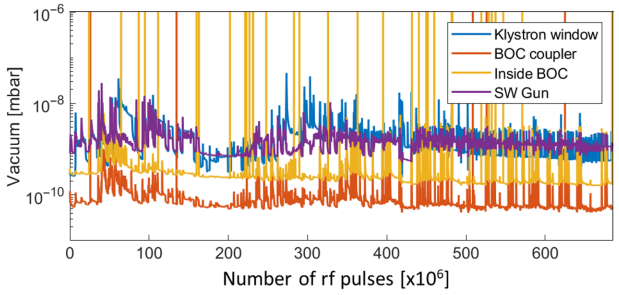

FIG. 21. Vacuum behavior as measured by the vacuum gauges distributed in the waveguide transport line and laser injection chamber during conditioning.

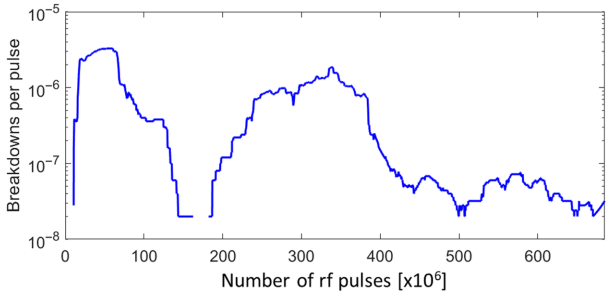

FIG. 22. Vacuum breakdown events in the gun and in the waveguide system during conditioning.

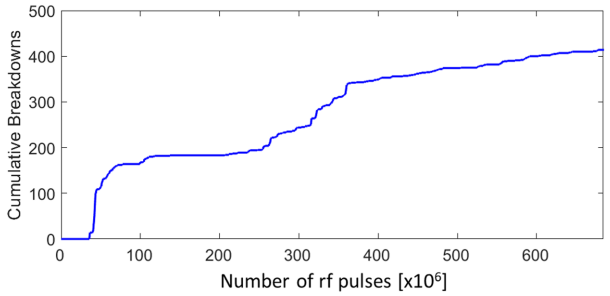

FIG. 23. Cumulative number of breakdown events.

input power we reached so far the calculated cathode peak field is ≈160 MV/m with no limitation due to breakdowns in the gun. The cumulative number of breakdown events is given in Fig. 23. The number of breakdown events in the gun has been estimated to be less than 10% of the total breakdown. In any case, the final measured total breakdown rate has been $\approx 2 \times 10^{-8}$ [bpp].

VII. CONCLUSIONS

A new SW C-band photogun has been designed, fabricated, and high-power tested with cathode peak fields of 160 MV/m without limitations due to the breakdown in the gun itself. The photogun's design is a 2.5-cell SW cavity with a four-port mode launcher, designed to operate with short rf pulses (300 ns) and high repetition rate (400 Hz). Its realization has been based on the new brazing-free technology developed and successfully tested at the National Institute of Nuclear Physics (INFN, Frascati, Italy). This device is extremely promising both for the achievable beam performance and for the possibility to operate at such high repetition rates. After the conclusion of this test, the gun will be installed in the INFN TEX Facility [31], where a 400 Hz C-band power station is being implemented, allowing full exploration of the C-band gun capabilities.

ACKNOWLEDGMENTS

We would like to acknowledge G. Castorina for the scientific support in mode launcher design and the COMEB Company for the technical support. This project has received funding from the European Union's Horizon 2020 Research and Innovation program under Grant Agreement No. 101004730 and by the INFN Commission Number V.

DATA AVAILABILITY

The data are not publicly available. The data are available from the authors upon reasonable request.

[1] J. Rosenzweig and E. Colby, Charge and wavelength scaling of rf photoinjector designs, AIP Conf. Proc. **335**, 724 (1995).

[2] V. A. Dolgashev, S. Tantawi, C. Nantista, Y. Higashi, and T. Higo, RF breakdown in normal conducting single-cell structures, in *Proceedings of the 2005 Particle Accelerator Conference* (IEEE, New York, NY, 2005), pp. 595–599.

[3] A. Giribono, D. Alesini, F. Cardelli, G. Di Raddo, L. Faillace, M. Ferrario, A. Gallo, A. Gizzi, S. Lauciani, A. Liedl *et al.*, Dynamics studies of high brightness electron beams in a normal conducting, high repetition rate C-band injector, Phys. Rev. Accel. Beams **26**, 083402 (2023).

[4] M. Ferrario, D. Alesini, M. Anania, M. Artioli, A. Bacci, S. Bartocci, R. Bedogni, M. Bellaveglia, A. Biagioni, F. Bisesto *et al.*, EuPRAXIA@SPARC_LAB design study towards a compact FEL facility at LNF, Nucl. Instrum. Methods Phys. Res., Sect. A **909**, 134 (2018).

[5] G. D'Auria, E. Adli, M. Aicheler, A. Aksoy, D. Alesini, R. Apsimon, J. Arnsberg, R. Auchettl, A. Bainbridge, K. Balazs *et al.*, The compactlight design study, Eur. Phys. J. Special Topics **233**, 1 (2024).

[6] C. J. Milne, T. Schietinger, M. Aiba, A. Alarcon, J. Alex, A. Anghel, V. Arsov, C. Beard, P. Beaud, S. Bettoni *et al.*, SwissFEL: The Swiss x-ray free electron laser, Appl. Sci. **7**, 720 (2017).

[7] T. Shintake *et al.*, A compact free-electron laser for generating coherent radiation in the extreme ultraviolet region, Nat. Photonics **2**, 555 (2008).

[8] https://ifast-project.eu/home.

[9] A. Grudiev, S. Calatroni, and W. Wuensch, New local field quantity describing the high gradient limit of accelerating structures, Phys. Rev. ST Accel. Beams **12**, 102001 (2009).

[10] V. Dolgashev, High magnetic fields in couplers of X-band accelerating structures, in *Proceedings of the 2003 Bipolar/BiCMOS Circuits and Technology Meeting (IEEE Cat. No. 03CH37440)* (IEEE, New York, NY, 2004), Vol. 2, pp. 1267–1269.

[11] D. Alesini, V. Lollo, and A. Battisti, International Patent Publication No. WO 2016/147118 A1, https://data.epo.org/publication-server/rest/v1.2/patents/EP3271622NWA1/document.html.

[12] V. A. Dolgashev, Progress on high-gradient structures, AIP Conf. Proc. **1507**, 76 (2012).

[13] W. Wuensch, Advances in high-gradient accelerating structures and in the understanding gradient limits, in *Proceedings of the IPAC-2017* (JACoW, Geneva, Switzerland, 2017), pp. 24–29.

[14] D. Alesini, A. Battisti, M. Ferrario, L. Foggetta, V. Lollo, L. Ficcadenti, V. Pettinacci, S. Custodio, E. Pirez, P. Musumeci *et al.*, New technology based on clamping for high gradient radio frequency photogun, Phys. Rev. ST Accel. Beams **18**, 092001 (2015).

[15] D. Alesini, A. Battisti, M. Bellaveglia, F. Cardelli, A. Falone, A. Gallo, V. Lollo, D. T. Palmer, L. Pellegrino, L. Piersanti *et al.*, Design, realization, and high power test of high gradient, high repetition rate brazing-free S-band photogun, Phys. Rev. Accel. Beams **21**, 112001 (2018).

[16] V. Shpakov, D. Alesini, M. Anania, M. Behtouei, B. Buonomo, M. Bellaveglia, A. Biagioni, F. Cardelli, M. Carillo, E. Chiadroni *et al.*, Design, optimization and experimental characterization of rf injectors for high brightness electron beams and plasma acceleration, J. Instrum. **17**, P12022

[17] D. Alesini, F. Cardelli, G. Castorina, M. Croia, M. Diomede, M. Ferrario, A. Gallo, A. Giribono, B. Spataro, C. Vaccarezza *et al.*, Design of a full C-band injector for ultra-high brightness electron beam, in *Proceedings of the 10th International Particle Accelerator Conference (IPAC-2019)* (JACoW, Geneva, Switzerland, 2019), pp. 1979–1982.

[18] D. Alesini, F. Cardelli, G. Di Raddo, L. Faillace, M. Ferrario, A. Gallo, A. Giribono, A. Gizzi, S. Lauciani, A. Liedl *et al.*, The new C band gun for the next generation rf photo-injectors, in *Proceedings of the IPAC-2022* (JACoW, Geneva, Switzerland, 2022), p. 679.

[19] D. Alesini, F. Cardelli, G. Di Raddo, L. Faillace, M. Ferrario, A. Gallo, A. Giribono, A. Gizzi, S. Lauciani, A. Liedl *et al.*, Progress on the new high gradient C band standing wave rf photo-gun, in *Proceedings of the IPAC-2023* (JACoW, Geneva, Switzerland, 2023), p. 1374.

[20] Canon Electron Tubes and Devices, https://etd.canon/en/product/category/microwave/klystron.html.

[21] L. Xiao, R. Boyce, D. Dowell, Z. Li, C. Limborg-Deprey, and J. Schmerge, Dual feed rf gun design for the LCLS, in *Proceedings of the 2005 Particle Accelerator Conference* (IEEE, New York, NY, 2005), pp. 3432–3434.

[22] G. Castorina, L. Ficcadenti, M. Migliorati, A. Mostacci, L. Palumbo, F. Cardelli, G. Franzini, A. Marcelli, B. Spataro, G. Sorbello *et al.*, A TM 01 mode launcher with quadrupole field components cancellation for high brightness applications, J. Phys. Conf. Ser. **1067**, 082025 (2018).

[23] G. Pedrocchi, M. Migliorati, A. Mostacci, L. Palumbo, L. Ficcadenti, R. INFN-Roma, I. G. Castorina, M. AVO-ADAM, S. D. Alesini, A. Gallo *et al.*, A C-band rf mode launcher with quadrupole field components cancellation for high brightness applications, in *Proceedings of the 12th International Particle Accelerator Conference (IPAC-2021), Campinas, Brazil* (JACoW, Geneva, Switzerland, 2021), pp. 3638–3641.

[24] C. Nantista, S. Tantawi, and V. Dolgashev, Low-field accelerator structure couplers and design techniques, Phys. Rev. ST Accel. Beams **7**, 072001 (2004).

[25] ANSYS electronics desktop, https://www.ansys.com/products/electronics.

[26] A. Giribono, D. Alesini, F. Cardelli, G. Castorina, G. D. Raddo, M. Ferrario, L. Ficcadenti, A. Gallo, G. Muti, G. Pedrocchi, J. Scifo, C. Vaccarezza, and A. Vannozzi, Effects of mode launcher on beam dynamics in next generation high brightness C-band guns, in *Proceedings of the IPAC-2021, International Particle Accelerator Conference No. 12* (JACoW, Geneva, Switzerland, 2021), pp. 813–816, 10.18429/JACoW-IPAC2021-MOPAB257.

[27] D. Alesini, M. Bellaveglia, S. Bini, A. Gallo, V. Lollo, L. Pellegrino, L. Piersanti, F. Cardelli, M. Migliorati, and A. Mostacci others, Design of high gradient, high repetition rate damped C-band rf structures, Phys. Rev. Accel. Beams **20**, 32004 (2017).

[28] SAES Getters S.p.A., https://www.saesgetters.com/highvacuum/solution/nextorr-d-z-uhv/.

[29] T. Lucas, C. Beard, P. Craievich, L. Hol, M. Pedrozzi, M. Zykova, R. Fortunati, R. Menzel, T. Kleeb, M. Schaer *et al.*, Developments and first results from an rf test stand for high brightness C-band photoguns at PSI, in *Proceedings of the IPAC-2024* (JACoW, Geneva, Switzerland, 2024), p. 2130.

[30] R. Zennaro, M. Bopp, A. Citterio, R. Reiser, and T. Stapf, C-band RF Pulse Compressor for SwissFEL, in *Proceedings of the International Particle Accelerator Conference, IPAC 2013, Shanghai, China* (2013).

[31] F. Cardelli, D. Alesini, M. Bellaveglia, S. Bini, B. Buonomo, S. Cantarella, M. Cianfrini, G. Catuscelli, C. Di Giulio, E. Di Pasquale *et al.*, Advancements in X-band technology at the TEX facility at INFN-LNF, in *Proceedings of the 14th International Particle Accelerator Conference* (JACoW, Geneva, Switzerland, 2024).